The Astrophysical Journal Supplement Series, 262:43 (12pp), 2022 October https://doi.org/10.3847/1538-4365/ac85e6

Optical Monitoring and Variability Analyses of the FSRQ 3C 454.3

Y. H. Yuan[1,2], G. G. Wang[1,2], H. B. Xiao[3], J. H. Fan[1,2], H. R. Huang[1,2], G. Z. Ding[1,2], G. Z. Wen[1,2], and F. J. Wu[1,2]
[1] Center for Astrophysics, Guangzhou University, Guangzhou, Guangdong, 510006, People's Republic of China; yh_yuan@gzhu.edu.cn
[2] Astronomy Science and Technology Research Laboratory of Department of Education of Guangdong Province, Guangzhou 510006, People's Republic of China
[3] Shanghai Key Lab for Astrophysics, Shanghai Normal University, Shanghai, 200234, People's Republic of China
Received 2022 May 11; revised 2022 July 28; accepted 2022 July 28; published 2022 September 27

Abstract

Based on the database monitored by the 1.26 m National Astronomical Observatory–Guangzhou University Infrared/Optical Telescope, we studied the optical variabilities of FSRQ 3C454.3. The monitoring period was from 2016 October 17 to 2018 December 14, and there were 6701 observations covering the *g*, *r,* and *i* bands (2196 at the *g* band, 2214 at the *r* band, and 2291 at the *i* band). (1) The maximum variabilities were $\Delta m_g = 2.806 \pm 0.124$ mag at the *g* band; $\Delta m_r = 2.365 \pm 0.160$ mag at the *r* band; and $\Delta m_i = 3.126 \pm 0.070$ mag at the *i* band. (2) Among the *gri* intraday lightcurves, there are 172 portions of the data sets showing intraday variability (IDV). The distributions of IDV timescales (ΔT) can be profiled by a three-order Gaussian function, with the center values $\Delta T_1 = 17.18$ minutes, $\Delta T_2 = 34.91$ minutes, and $\Delta T_3 = 68.92$ minutes. These results imply that the origin of IDVs is very complicated. (3) Based on the IDV timescales, we obtained the emission size $R \leqslant 7.17 \times 10^{15}$ cm, fixed the broad-line region and modeled the spectral energy distributions. (4) We used the Jurkevich method, red-noise fitting, and the weighted wavelet Z-transform to analyze the long-term variabilities and obtained indications of a possible period of $P = 2.92 \pm 0.85$ yr, and used the binary black hole system to explain this period. Based on the long-term period, we can estimate the time until merger of the binary black hole, $t_{\rm merge} = 6.69 \times 10^3$ yr, and the luminosity of gravitational waves, $L_G = 1.56 \times 10^{48}$ erg s^{-1}.

Unified Astronomy Thesaurus concepts: Galaxies (573); Blazars (164); CCD photometry (208)

Supporting material: machine-readable tables

1. Introduction

Blazars show some extreme properties, such as violently optical variability, core dominance, superluminal motion, and so on (Urry & Padovani 1995; Ulrich et al. 1997; Fan 2005). Blazars can be divided into two subclasses, BL Lac objects and flat-spectrum radio spectrum (FSRQs), among which, the former one is characterized by featureless optical spectra or weak emission lines (Stickel et al. 1991), and the latter one is composed of the flat-spectrum radio spectrum and the typical broad emission lines (Urry & Padovani 1995).

Optical variabilities with the timescales from minutes to years are very typical characteristics of blazars, and play a very important role in distinguishing blazars from the other active galactic nuclei (AGNs). As a main result in the optical analysis, variable timescales can be divided into three types: the first one is microvariability (intraday variability (IDV)), with the timescales within 1 day; the second one is short-term variability, with the timescales from days to months; the last one is long-term variability, with the timescales of years (Fan 2005).

Most of the IDVs are nonperiodic, and might originate from the instability of accretion disk, the jets, or the interstellar medium, and so on. But, there are some blazars showing periodic IDVs. For example, OJ 287 displayed a period of ~40 minutes at radio band in Visvanathan & Elliot (1973); Valtaoja et al. (1985) reported a possible period of 15.7 minutes at radio band; Kinzel et al. (1988) obtained a period of 35 minutes in the 7 mm lightcurve. For 3C 454.3, Fan et al. (2019) found a IDV period of 102 minutes based on the optical lightcurve. Yuan & Fan (2021) obtained that BL Lac object PKS 0735+178 had intraday periodic oscillations with the period $P = 66.9 \pm 4.1$ minutes. Liu et al. (2021) reported that for S5 0716+714, the IDV period was ≈ 185.78 minutes; for 3C 273, the IDV periods were ~60 and ~80 minutes.

3C454.3 is an FSRQ, with the redshift $z = 0.859$ (Jackson & Browne 1991). This source is one of the brightest blazars and nicknamed as a "Crazy Diamond" (Vercellone et al. 2010). Over the whole electromagnetic wavelength, 3C454.3 displays violent variabilities (Bennett 1962; Sandage 1966; Blom et al. 1995; Hartman et al. 1999; Tavecchio et al. 2002; Bennett et al. 2003; Zhang et al. 2005; Fan et al. 2019, 2021; Amaya-Almazán et al. 2021; Sarkar et al. 2021, and references therein).

Tritton & Selmes (1971) reported a variation of 1.5 mag during a period of 500 days. Raiteri et al. (1998b) gave a brightness decrease of 0.15 mag at the *R* band and a brightness variation of 0.06 mag at the *V* band within 1.7 hr. Xie et al. (2001) put forward a variable value of 0.61 mag within 7 minutes. The violent variation Δm = 2.3 mag was reported by Angel & Stockman (1980), and the variability of about 0.5 mag within 1 day was put forward by Lloyd (1984). In the monitoring duration of 2000 October, Fan et al. (2004) used the 70 cm telescope at Abstumani Observatory in Georgia to monitor this source, but did not find clear variability. In 2001, this source became brighter in the optical band, and, in 2005, this source reached the brightest value $R = 12.0$ mag (Fuhrmann et al. 2006; Giommi et al. 2006; Pian et al. 2006; Villata et al. 2006). Gaur et al. (2012) studied the observations during the period from 2009 to 2010, and obtained IDVs within four nights. This source is an important monitored target in our monitoring programs at Xinglong Station of National

Table 1
Comparison Stars of 3C454.3

Comp (1)	U(error) (mag) (2)	B(error) (mag) (3)	V(error) (mag) (4)	R(error) (mag) (5)	I(error) (mag) (6)	g (mag) (7)	r (mag) (8)	i (mag) (9)
A	17.39 (0.05)[a]	16.85 (0.05)[a]	15.86 (0.09)[b]	15.32 (0.09)[b]	14.80 (0.06)[b]	16.38	15.49	14.86
C	15.42 (0.02)[a]	15.18 (0.02)[a]	14.43 (0.02)[a]	13.98 (0.02)[c]	13.51 (0.02)[c]	14.80	14.12	13.54
D	15.94 (0.02)[a]	14.94 (0.02)[a]	13.85 (0.02)[a]	13.22 (0.01)[c]	12.63 (0.01)[c]	14.42	13.33	12.68
E	18.94 (0.14)[a]	17.10 (0.14)[a]	15.76 (0.09)[b]	14.92 (0.08)[b]	14.26 (0.08)[b]	16.48	15.01	14.33
F	16.35 (0.11)[a]	16.06 (0.11)[a]	15.21 (0.11)[a]	14.83 (0.03)[d]	...	15.70	14.86	14.03
G	16.71 (0.08)[a]	16.28 (0.08)[a]	15.42 (0.08)[a]	14.83 (0.02)[d]	...	15.94	14.90	13.87
H	15.17 (0.02)[a]	14.62 (0.02)[a]	13.65 (0.04)[b]	13.10 (0.04)[b]	12.58 (0.04)[b]	14.13	13.24	12.61

Notes. Column (7): g magnitude, in units of magnitude. Column (8): r magnitude, in units of magnitude. Column (9): i magnitude, in units of magnitude.
[a] Angione (1971).
[b] Fiorucci et al. (1998).
[c] Smith & Balonek (1998).
[d] Raiteri et al. (1998a).

Astronomical Observatory, Shanghai Astronomical Observatory, and Abstumani Observatory (Fan et al. 2004, 2014a, 2017, 2019, 2021; Tao et al. 2008; Kurtanidze et al. 2009).

Vittorini et al. (2014) put forward a theoretical framework to explain multiband emission of 3C 454.3 and model the spectral energy distributions (SEDs) for different states. Based on the R lightcurve monitored by several ground-based telescopes, Weaver et al. (2019) reported a typical period of 36 minutes, and found the size of emission region $r \leqslant 2.6 \times 10^{15}$ cm.

In order to analyze the optical variabilities, we carried out the observations using the 1.26 m National Astronomical Observatory–Guangzhou University Infrared/Optical Telescope (NGT). This paper is arranged as follows: in Section 2, we show the observations and data reductions; in Section 3, we analyze optical variability; in Section 4, we present the predicted spectra of the SED; in Section 5, we present a discussion and conclusions.

2. Data Reductions and Observations

2.1. Photometry Process

NGT is located at Xinglong station, National Astronomical Observatories, Chinese Academy of Sciences. This telescope is equipped with three SBIG STT-8300M cameras with a CCD of 3326×2504 pixels and a field of view of $6'.0 \times 4'.5$. This filters adopt standard Sloan Digital Sky Survey g, r, and i bands. The detailed description about this telescope was shown in Fan et al. (2019).

We use the following procedures to make the image reduction.

1. Obtain the bias images at the beginning and the end of the observation night.
2. Take the flat-field images at dusk and dawn.
3. Photometric observations are obtained after the bias and flat-field corrections.

2.2. Standard Stars

Based on available literature (Angione 1971; Fiorucci et al. 1998; Smith & Balonek 1998 and Raiteri et al. 1998a), we collected the standard stars, and noted them as “A, C, D, E, F, G, and H.” The comparison stars have been listed in Table 1, where Column (1) lists the order number of the comparison stars and Columns (2)–(6) list comparison stars at the U, B, V, R, and I bands, in units of magnitude.

Based on the least-squares fitting method, $M_\nu = a\log^2\nu + b\log\nu + c$—here, M_ν is the magnitude at the ν band ($\nu = U$, B, V, R, and I)—we calculated the g, r, and i magnitudes of every comparison star. The fitting processes have been noted in Figure 1; here, the black solid dots stand for the U, B, R, V, and I magnitudes, the red solid dots stand for g, r, and i magnitudes, and the red lines stand for the least-squares fitting curves. The fitting results are noted in Table 1.

2.3. Data Reductions

Within the same frame, for each comparison star c_i, $i = 1 - n$, we obtain the magnitude m_i for the object of interest. At the given time, the object magnitude should be

$$\overline{m} = \frac{\sum m_i}{N}. \quad (1)$$

Here, N is the total number of comparison stars. The corresponding uncertainty σ can be calculated by

$$\sigma = \sqrt{\frac{\sum(m_i - \overline{m})^2}{N - 1}}. \quad (2)$$

2.4. Observations

Within the 67 observational nights from 2016 October 17 to 2018 December 14, we carried out the photometric observations. Based on the above processes, we performed the data reduction and presented the results in Figure 2, where the black solid dots stand for g lightcurve, the red solid dots stand for r lightcurve, and the green solid dots stand for i lightcurve.

The observations have been listed in Table 2.

3. Optical Variabilities

3.1. Intraday Optical Variabilities

3.1.1. Techniques

There are many methods using to constrain the IDVs (Heidt & Wagner 1996; Romero et al. 1999; de Diego 2010), which can be introduced as the following.

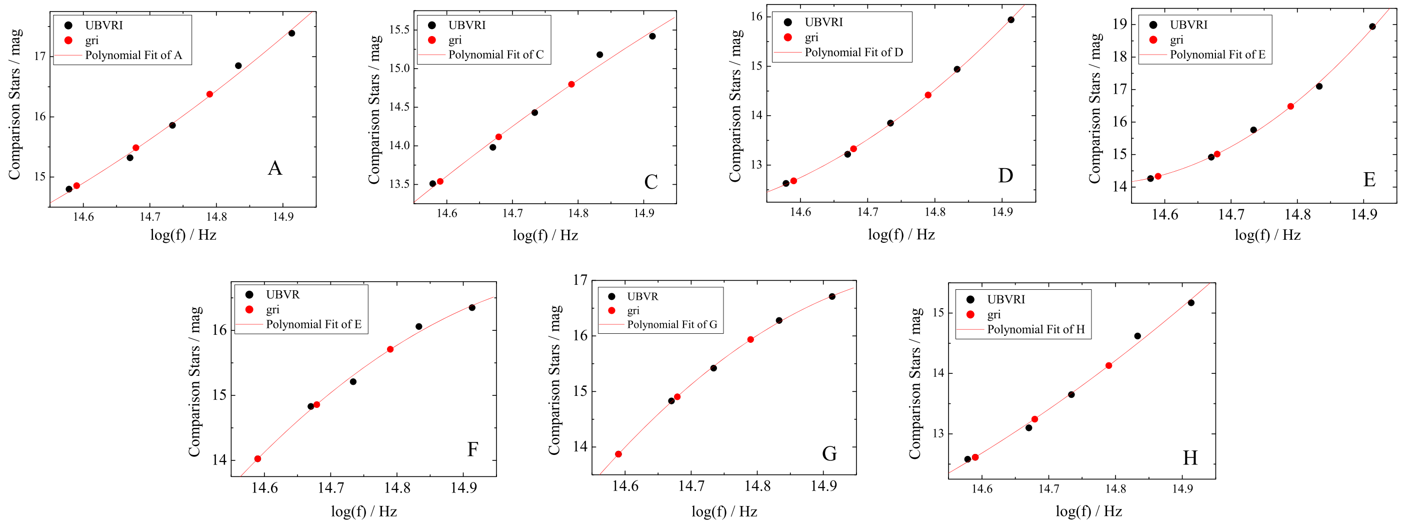

Figure 1. The g, r, and i fitting results of the seven comparison stars. The black solid dots stand for U, B, V, R, and I data, the red solid dots stand for g, r, and i data, and the red lines stand for the least-squares fitting curves.

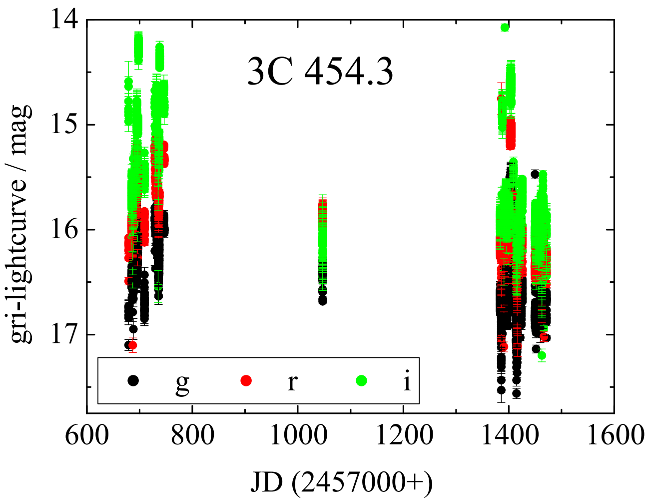

Figure 2. The g, r, and i lightcurves. The black solid dots stand for the g lightcurve, the red solid dots stand for the r lightcurve, and the green solid dots stand for the i lightcurve.

1. Heidt & Wagner (1996) pointed out a variability amplitude parameter (A_m),

$$A_m = 100 \times \sqrt{(m_m - m_n)^2 - {\sigma_m}^2 - {\sigma_n}^2}\,(\%).$$

   Here, m_m is the maximum value, m_n is the minimum value, and σ_m and σ_n are the corresponding uncertainties. When $A_m > 7.5\%$, the source is variable.
2. *F-test.*

   De Diego (2010) introduced this method, which can be used to study the significance of a variation. This method can be determined by $F = \frac{S_o^2}{S_t^2}$, where S_o^2 is the variance of the object differential lightcurve values and S_t^2 is the variance of the differential lightcurve values of the comparison stars.
3. *Nested ANOVA.*

   The ANOVA test can compare the means of dispersion among the different groups of observations. The nested ANOVA test is an updated ANOVA test that can generate the different lightcurves of blazars based on several stars as the reference stars. The detailed introduction about this method are shown in de Diego et al. (2015).

   For each intraday lightcurve, the number of freedom degrees (ν_O and ν_C) are the same and equal to $N-1$; here, N is the pair number of observations. In order to check the variable values of a target, we can compare the F value from the observations with the critical value, $F_{C(\nu_O,\nu_C)}$. The F-test can be determined within two significance levels (1% and 0.1%). This method is consistent with the 2.6σ and 3σ detections respectively (De Diego 2010; Fan et al. 2017; Xiong et al. 2017).
4. Variability values and variability timescales.

On one single day, if there is an IDV, we use the following procedure to obtain the variable values ($\Delta m \pm \sigma$) and variable timescales (ΔT).

The intraday lightcurves are divided into some specific stages (brightening stages or dimming stages), which have been noted in Figure 3, Figure 4, and Figure 5, and noted by "1," "2," "3,"... At every stage, we calculate the most violent variability ($\Delta m \pm \sigma$); if $\Delta m > 2\sigma$, then, $\Delta m \pm \sigma$ is the variable values, and the corresponding time span is the variable timescales (ΔT). We use a linear regression to fit the relations between the timescale and magnitude variation, seeing the colored lines in Figures 3–5.

3.1.2. Results

The calculation results are listed in Tables 3–5, with the column labels defined under each table.

At the g band, within 11 days, there are 24 stages displaying IDVs, with the variable timescales from 14.40 to 216 minutes and the averaged value $\overline{\Delta T} = 66.67 \pm 49.66$ minutes. The variable value (Δm) are in the range from 0.09 ± 0.03 to 0.81 ± 0.16 mag, with the averaged value $\overline{\Delta m_g} = 0.294 \pm 0.204$ mag.

At the r band, within 39 days, there are 104 stages displaying IDVs, with the variable timescales from 5.76 to 210.24 minutes, and averaged value $\overline{\Delta T} = 57.41 \pm 39.06$ minutes. The variable values (Δm) are in the range from 0.04 ± 0.006 mag to 1.203 ± 0.091 mag, with the averaged value $\overline{\Delta m_r} = 0.197 \pm 0.175$ mag.

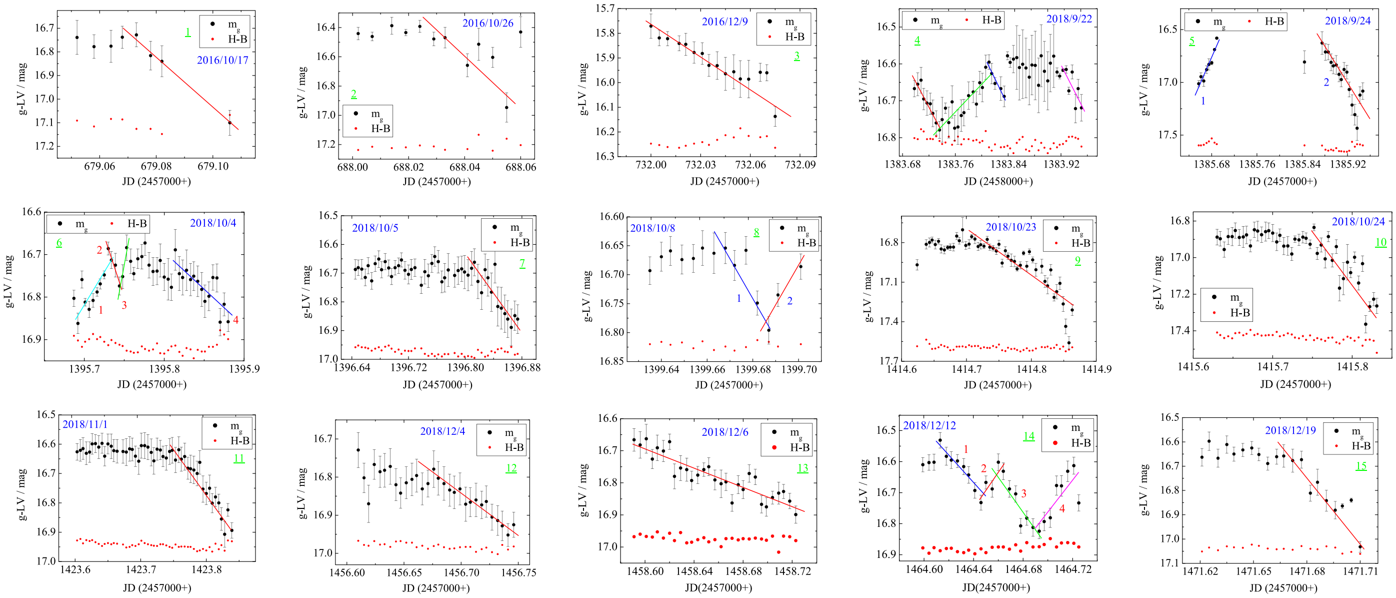

Figure 3. The intraday optical variabilities at the g band.

Table 2
The gri Observations of 3C454.3

g-JD (+2,457,000) (1)	m_g (mag) (2)	σ_g (mag) (3)	r-JD (+2,457,000) (4)	m_r (mag) (5)	σ_r (mag) (6)	i-JD (+2,457,000) (7)	m_i (mag) (8)	σ_i (mag) (9)
679.052	16.74	0.07	679.052	16.15	0.03	679.052	14.88	0.10
679.058	16.78	0.05	679.058	16.13	0.02	679.058	14.85	0.07
679.064	16.78	0.07	679.064	16.12	0.02	679.064	14.85	0.09
679.068	16.74	0.05	679.068	16.08	0.02	679.068	14.91	0.09
679.073	16.73	0.05	679.073	16.20	0.03	679.073	14.97	0.10

Notes. Column (1): g-JD, +2,457,000. Column (2): m_g, in units of magnitude. Column (3): σ_g, uncertainty for m_g, in units of mag. Column (4): r-JD, +2,457,000. Column (5): m_r, in units of magnitude. Column (6): σ_r, uncertainty for m_r, in units of magnitude. Column (7): i-JD, +2,457,000. Column (8): m_i, in units of magnitude. Column (9): σ_i, uncertainty for m_i, in units of magnitude.
At the g band, there are 2196 observations giving a largest variation with $\Delta m_g = 2.81 \pm 0.12$ mag. At the r band, there are 2214 observations, with $\Delta m_r = 2.37 \pm 0.16$ mag. At the i band, there are 2291 observations, with $\Delta m_i = 3.13 \pm 0.07$ mag.

(This table is available in its entirety in machine-readable form.)

At the i band, within 16 days, there are 44 stages displaying IDVs, with the variable timescales from 7.2 to 223.20 minutes and the averaged value $\overline{\Delta T} = 57.47 \pm 50.39$ minutes. The variable values (Δm) are in the range from 0.04 ± 0.01 to 1.29 ± 0.09 mag, with the averaged value $\overline{\Delta m_i} = 0.344 \pm 0.262$ mag.

3.2. Long-term Optical Variabilities

There are many blazars, such as OJ 287, 3C 273, 3C 446 PKS 2251+158, etc, showing a quasiperiodic phenomenon in their long-term lightcurves. We combine our observations with the data collected from the available literature, and then build the study sample. The literature is Angione (1968), Webb et al. (1988), Villata et al. (2001), Gu et al. (2006), Raiteri et al. (2007), Raiteri et al. (2008), Bachev et al. (2011), Ogle et al. (2011), Fan et al. (2018), Fan et al. (2021), the Small and Moderate Aperture Research Telescope System, and the Steward Observatory blazar monitoring program. All the data are shown in Figure 6, where the black dots stand for the data from the literature, and the red dots stand for our observations. In order to improve the efficiency of the calculation, we calculated the averaged lightcurves of those with the bin of 1 day. So, in the following analysis of the long-term variabilities, we used the averaged lightcurves, which cover about 118 yr.

For blazars, it is very difficulty to constrain the periodic signals because of the uneven distributions of observations (Vaughan et al. 2016). So, we choose more than one method to study the periodic properties and obtain the periodic signal when the results from different methods are consistent with each other in the error range.

In this work, we choose Jurkevich (JV), power spectrum (red-noise fitting (REDFIT)), and the weighted wavelet Z-transform (WWZ) to search for the quasiperiodicities. These methods are introduced as follows.

1. *Jurkevich results.*
The Jurkevich method (Jurkevich et al. 1971) is based on the expected mean square deviation (V_m^2). It tests a run of trial periods (P) around which the data are folded. All data are assigned to m groups according to their phases around each bin. The trial periods should be a true period when V_m^2 reaches the minimum. Kidger et al. (1992) put forward a judgement criteria of the period, $f = \frac{1 - V_m^2}{V_m^2}$. When $f \geqslant 0.5$, the period is very strong; when

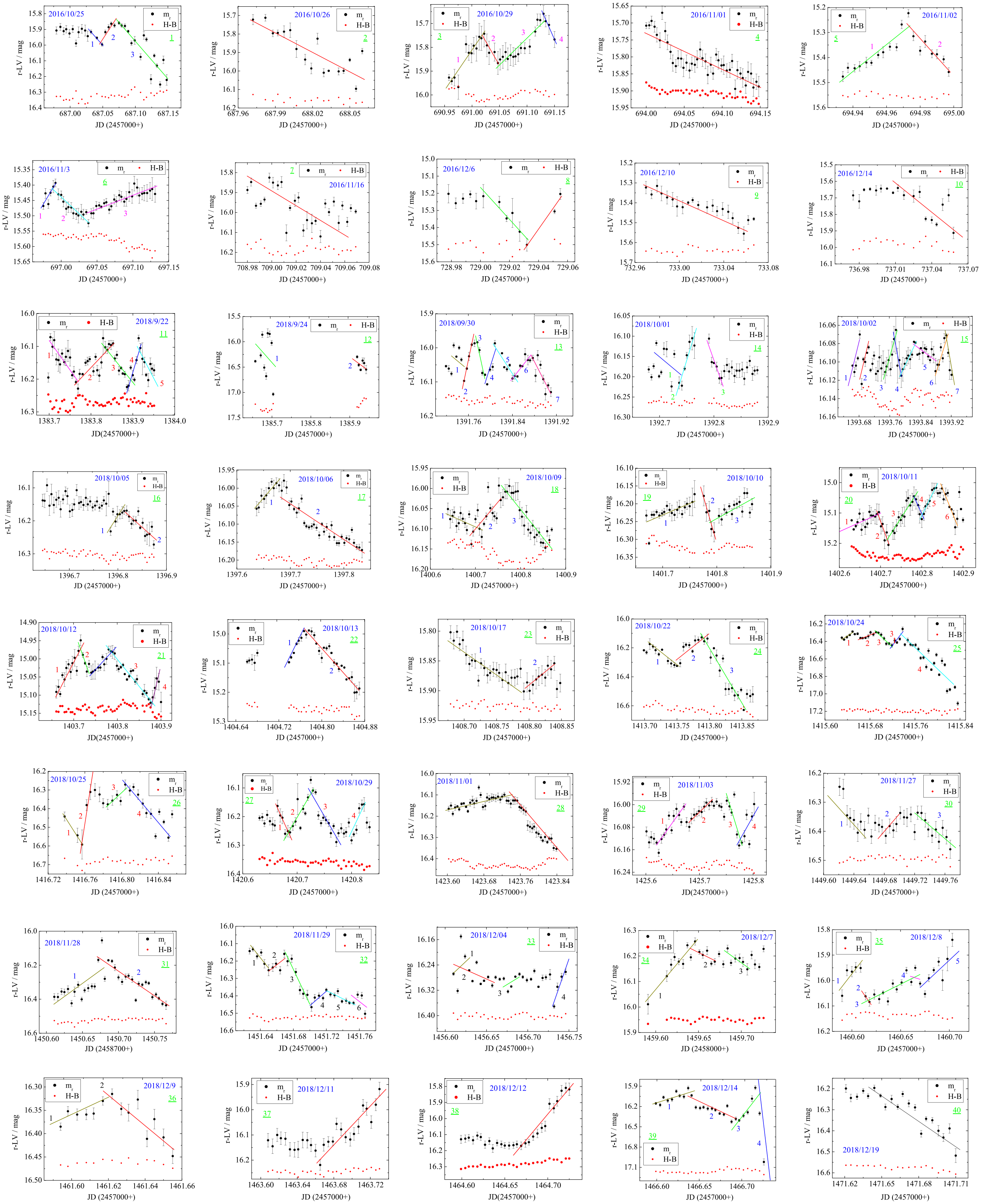

Figure 4. The intraday optical variabilities at the r band.

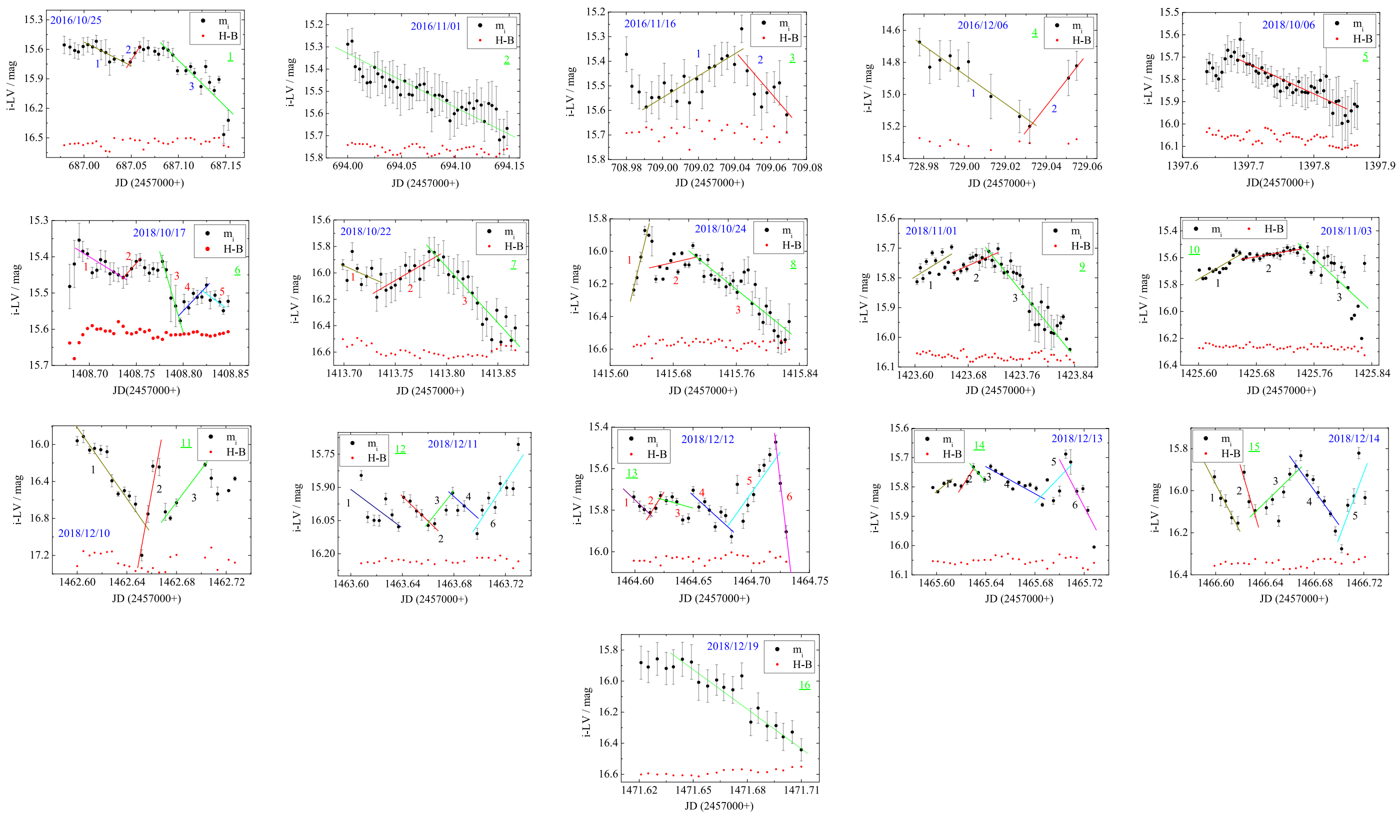

Figure 5. The intraday optical variabilities at the i band.

Table 3
The IDV Results of FSRQ 3C454.3 at the g Band

Date	N	Am	$\overline{F}$	ANOVA	$F^c_{(99)}$	$F^c_{(99.9)}$	Note	ΔT (minutes)	$\Delta m \pm \sigma$ (mag)	$\frac{\Delta m}{\sigma}$
(1)	(2)	(3)	(4)	(5)	(6)	(7)	(8)	(9)	(10)	(11)
2018/12/19	20	43.28	4.47	20.03	3.02	4.47	V	62.58	0.44 ± 0.04	9.89
2018/12/12	29	…	…	4.13	…	…	…	…	…	…
1	9	5.74	9.43	...	6.02	12.04	V	47.52	0.20 ± 0.04	5.74
2	6	3.61	6.59	...	…	…	V	20.16	0.13 ± 0.04	3.61
3	9	6.17	11.12	...	6.03	12.04	V	47.52	0.22 ± 0.04	6.17
4	8	5.86	8.53	...	6.99	15.01	V	40.32	0.21 ± 0.04	5.86
2018/12/11	27	…	…	…	2.55	3.53	N	…	…	…
2018/12/9	15	1.71	1.06	0.81	3.70	5.93	N	…	…	…

Note. Column (1): Date. Column (2): N. Column (3): Am. Column (4): $\overline{F}$. Column (5): ANOVA. Column (6): $F^c_{(99)}$. Column (7): $F^c_{(99.9)}$. Column (8): Note, "V": variable, "N": nonvariable, "P": possible variable. Column (9): ΔT, in units of minutes. Column (10): $\Delta m \pm \sigma$, in units of magnitude.

(This table is available in its entirety in machine-readable form.)

$0.5 \geqslant f \geqslant 0.25$, there might lie a period. Based on the Jurkevich method, we obtain three likely periodic signals, $P_1 = 2.99 \pm 0.73$ yr, $P_2 = 6.97 \pm 0.75$ yr, and $P_3 = 9.33 \pm 1.12$ yr, see Figure 7.

2. *REDFIT results.*

The REDFIT program used in this work is cited from Schulz & Mudelsee (2002), which is based on the Lomb–Scargle periodogram (Lomb 1976; Scargle 1982). The error can be obtained by the FWHM. The red-noise spectrum used to judge the REDFIT results is based on a first-order autoregressive (AR1).

Based on the REDFIT method, the analyzed result has been shown in Figure 8, where the black line stands for the power spectrum signal; the red line, the green line, the blue line, the cyan line, and the magenta line stand for the 70%, 80%, 90%, 95%, and 99% red-noise level, respectively. From Figure 8, we can see three signals, $P = 3.30 \pm 0.56$ yr, 1.17 ± 0.12 yr, and 87.72 ± 3.40 days, exceed to a 70% red-noise level, which might be three periodic signals of variability.

3. *WWZ results.*

Foster (1996a) applied the Z-statistic of Foster (1996b) to deduce the WWZ, which was based on the wavelet analysis and vector projection, and can effectively

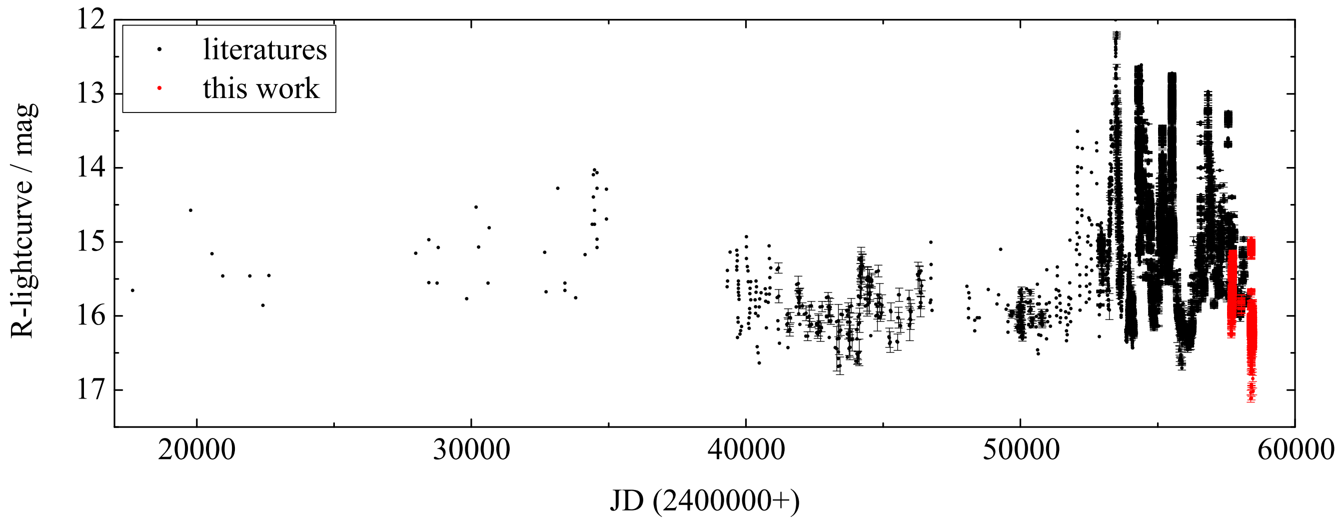

Figure 6. The long-term lightcurve of 3C 454.3, where the black dots stand for the data collected from the literature and the red dots stand for the observations from this work.

Table 4
The IDV Results of FSRQ 3C454.3 at the r Band

Date	N	Am	$\overline{F}$	ANOVA	$F^c_{(99)}$	$F^c_{(99.9)}$	Note	ΔT (minutes)	$\Delta m \pm \sigma$ (mag)	$\frac{\Delta m}{\sigma}$
(1)	(2)	(3)	(4)	(5)	(6)	(7)	(8)	(9)	(10)	(11)
2018/12/19	20	32.00	5.14	13.463	3.03	4.47	V	95.04	0.32 ± 0.04	9.20
2018/12/14	28	…	…	3.045	2.51	3.44	…	…	…	…
1	10	24.70	6.53	...	5.35	10.11	V	47.52	0.25 ± 0.04	6.41
2	12	49.65	5.03	...	4.46	7.76	V	73.44	0.50 ± 0.04	13.11
3	7	50.14	12.25	...	8.46	20.03	V	40.32	0.50 ± 0.04	12.58
4	3	109.66	24.26	...	…	…	V	14.40	1.10 ± 0.06	19.96
2018/12/12	15	9.50	7.15	12.278	3.69	5.93	V	74.88	0.36 ± 0.04	9.50
2018/12/11	27	29.91	1.46	10.853	2.55	3.53	V	93.60	0.30 ± 0.03	8.85
2018/12/9	14	…	…	5.487	3.91	6.41	…	…	…	…
1	7	6.87	2.17	...	8.47	20.03	V	40.32	0.07 ± 0.01	5.00
2	8	13.16	24.11	...	6.99	15.02	V	47.52	0.13 ± 0.02	7.00

Note. Column (1): Date. Column (2): N. Column (3): Am. Column (4): $\overline{F}$. Column (5): ANOVA. Column (6): $F^c_{(99)}$. Column (7): $F^c_{(99.9)}$. Column (8): Note, "V": variable, "N": nonvariable, "P": possible variable. Column (9): ΔT, in units of minutes. Column (10): $\Delta m \pm \sigma$, in units of magnitude.

(This table is available in its entirety in machine-readable form.)

Table 5
The IDV Results of FSRQ 3C454.3 at the i Band

Date	N	Am	$\overline{F}$	ANOVA	$F^c_{(99)}$	$F^c_{(99.9)}$	Note	ΔT (minutes)	$\Delta m \pm \sigma$ (mag)	$\frac{\Delta m}{\sigma}$
(1)	(2)	(3)	(4)	(5)	(6)	(7)	(8)	(9)	(10)	(11)
2018/12/19	20	57.08	16.25	32.405	3.03	4.47	V	95.04	0.59 ± 0.13	4.57
2018/12/14	27	…	…	1.380	2.55	3.53	…	…	…	…
1	5	21.59	14.38	...	15.98	53.44	V	27.36	0.22 ± 0.04	5.24
2	3	17.78	7.41	...	98.99	998.99	V	12.96	0.18 ± 0.04	4.26
3	9	30.91	5.35	...	6.03	12.05	V	25.92	0.31 ± 0.04	8.89
4	9	35.76	6.46	...	6.03	12.05	V	40.32	0.36 ± 0.03	11.58
5	5	45.38	7.40	...	15.98	53.44	V	20.16	0.46 ± 0.03	13.38

Note. Column (1): Date. Column (2): N. Column (3): Am. Column (4): $\overline{F}$. Column (5): ANOVA. Column (6): $F^c_{(99)}$. Column (7): $F^c_{(99.9)}$. Column (8): Note, "V": variable, "N": nonvariable, "P": possible variable. Column (9): ΔT, in units of minutes. Column (10): $\Delta m \pm \sigma$, in units of magnitude.

(This table is available in its entirety in machine-readable form.)

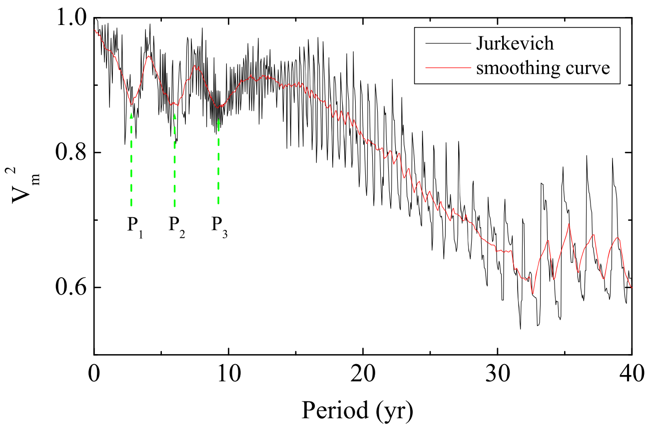

Figure 7. The quasi-period calculated by the Jurkevich method. The black line stands for the Jurkevich result and the red line stands for the smoothing curve.

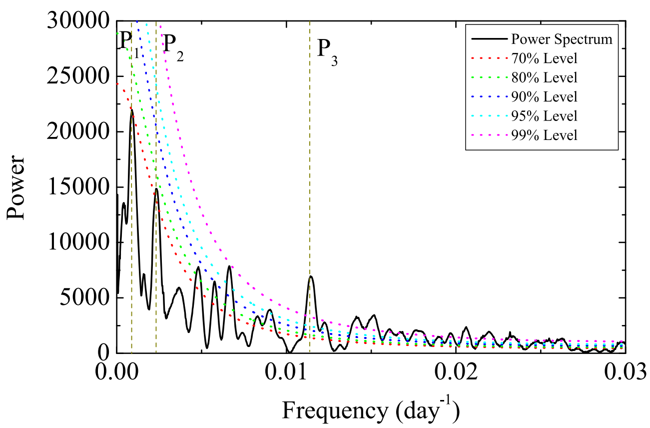

Figure 8. The quasi-period calculated by the power spectrum. The black line stands for the signal and the colorful dot lines stand for the theoretical red-noise spectra of 70%, 80%, 90%, 95%, and 99% significance level respectively.

study the nonuniform signals and conveniently major in time-frequency local characteristic analysis.

Based on the WWZ method, the result has been shown in Figure 9, where the left panel stands for the 2D plane contour of the WWZ, and the right panel stands for the time-averaged WWZ power spectrum. The result displays a clear peak $P = 2.92 \pm 0.85$ yr (the uncertainty from the Gaussian fitting).

We note that all three analysis methods, Jurkevich, REDFIT, and WWZ, give indications of a consistent quasi-period around 2.92 ± 0.85 yr, see Table 6. This is shown as a blue dashed curve in Figure 10, but it is clearly not a good fit to the sparser earlier data. In addition, this signal is not very strong when compared to the red-noise via the REDFIT method, and there is a much stronger REDFIT signal in the periodogram around 88 days. Further, the WWZ signal is significant for a span of around only 3000 days, so a convincing claim of a roughly 1000 day quasiperiodic oscillation (QPO) cannot really be obtained from that approach. The nominal presence of similar periodic signals obtained by quite different methods hints that there could be something real there, but no strong claim can be made.

4. The Predicted Spectra of the Spectral Energy Distribution

There are some works (Vercellone et al. 2010; Vittorini et al. 2014; Sahakyan 2021) to model the SEDs of 3C 454.3 during

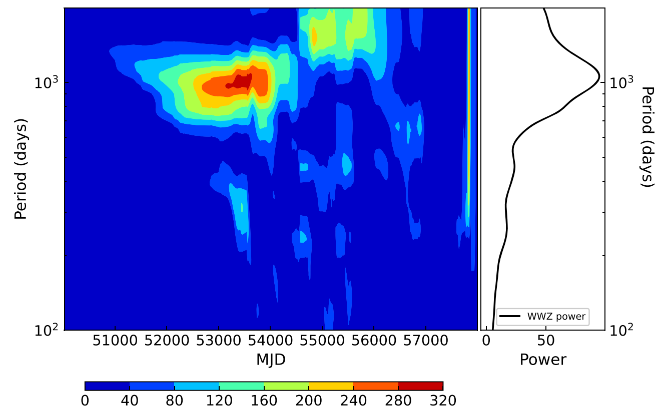

Figure 9. The quasi-period calculated by the weighted wavelet Z-transform (WWZ), where, the left panel stands for the two-dimensional contour map of WWZ, and the right panel stands for the time-averaged WWZ power.

Table 6
The Period of the Long-term Lightcurves

Method (1)	Result (2)	Period (3)
WWZ	2.92 ± 0.85 (yr)	...
REDFIT	3.30 ± 0.56 (yr), 1.17 ± 0.12 (yr), 87.72 ± 3.40 (days)	2.92 ± 0.85 (yr)
JV	2.99 ± 0.73 (yr), 5.97 ± 0.75 (yr), 9.33 ± 1.12 (yr)	...

the different states. In Section 5.2, we obtain the timescales of intraday optical variabilities in the range from 7.2 to 223.20 minutes. If the intraday variable timescales are dominated by the light travel time and the size of the emission region can be constrained by the variable timescales ΔT,

$$R \leqslant \frac{c\delta\Delta T}{1+z}.$$

If we consider the maximum timescale $\Delta T = 223.2$ minutes, $z = 0.859$, $\delta = 33.2$ (Hovatta et al. 2009), we can obtain the emission region $R \leqslant 7.17 \times 10^{15}$ cm.

If the movement of relativistic motion of the plasmoid along the jet causes the γ-ray radiation by external Compton (EC) radiation from the origin electron originated by the broad-line region (BLR) with timescales ($\Delta t_{\rm obs}$) (Vittorini et al. 2014),

$$\Delta t_{\rm obs} = (1 - \beta\cos\theta)\frac{R_{\rm BLR}}{c}.$$

When the viewing angle $\theta \sim \Gamma^{-1}$, we can obtain that the region of BLR should be $R_{\rm BLR} \simeq \Delta t_{\rm obs} \cdot c \cdot \Gamma^2$. Based on $\Gamma \approx 20$ (Vercellone et al. 2010), $\Delta t_{\rm obs} \in (7.2, 223.2)$ minutes, we can obtain $R_{\rm BLR} \approx (0.5 \sim 16.1) \times 10^{16}$ cm. Costamante et al. (2018) pointed out $R_{\rm BLR} \simeq 5.8 \times 10^{17}$ cm. So the region of BLR can be constrained as $0.5 \sim 58(\times 10^{16})$ cm.

We build an SED, which combines our observations and the data collected from the NASA/IPAC Extragalactic Database (NED),[4] as shown in Figure 11, where the red dots stand for our observations and the black dots stand for the collected data. We avail the AGN SED tool[5] to build the SED (Massaro et al. 2006; Tramacere et al. 2009, 2011). The fitting parameters are

[4] http://ned.ipac.caltech.edu/
[5] From https://www.isdc.unige.ch/sedtool/PROD/SED.html.

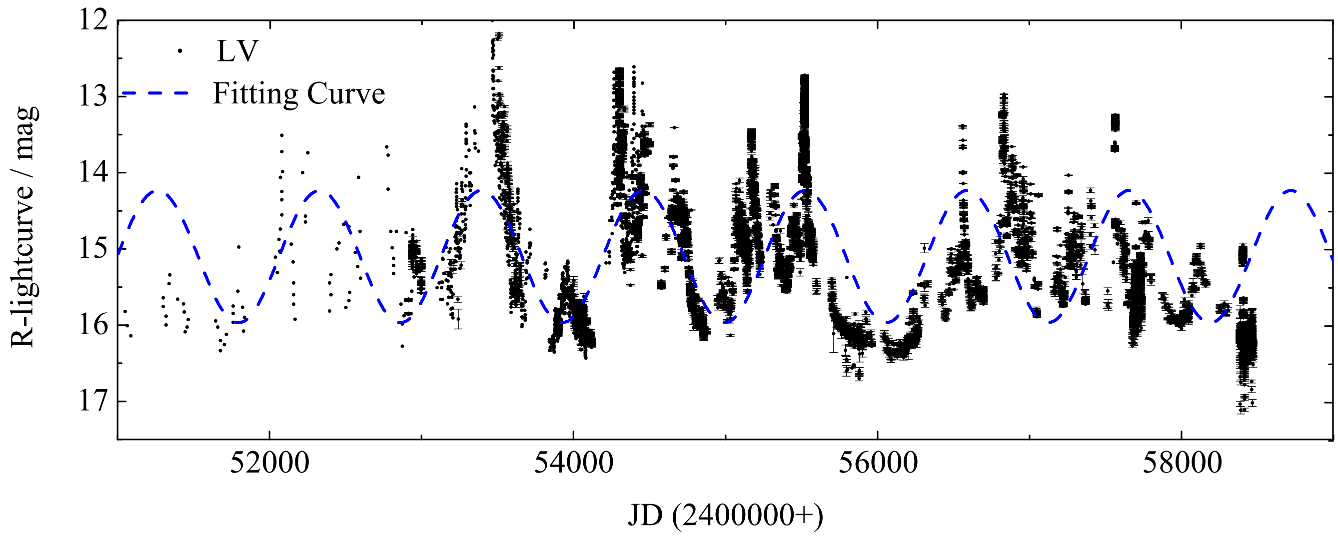

Figure 10. The fitting curve for the long-term lightcurve based on a sine function. The black dots stand for the lightcurves and the blue dash curve stand for the fitting curve.

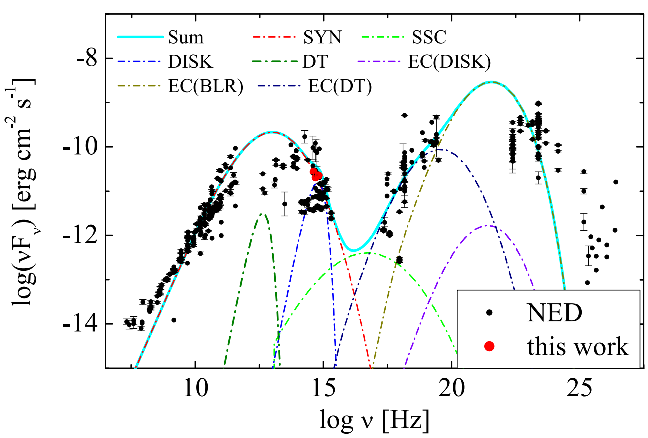

Figure 11. Comparisons of the predicted multiwavelength spectra of 3C 454.3 using the observations from this work (red dots) and NED (black dots). The red, green, blue, olive, violet, dark yellow, and navy dotted–dashed lines stand for the synchrotron, SSC, thermal (DISK), thermal (DT), EC (DISK), EC (BLR) and EC (DT) spectra respectively. The cyan line stands for the combination of the upper total spectra.

listed in Table 7, and the predicted spectra are shown in Figure 11, where

1. The red dotted–dashed curve stands for the predicted synchrotron spectrum (SYN),
2. The green dotted–dashed curve stands for the synchrotron self-Compton (SSC),
3. The blue dotted–dashed curve stands for the thermal spectrum of accretion disk (DISK),
4. The olive dotted–dashed curve stands for the thermal spectrum of dusty (DT),
5. The violet dotted–dashed curve stands for the external inverse Compton from the accretion disk (EC (DISK)),
6. The dark yellow dotted–dashed curve stands for the external inverse Compton from the BLR (EC (BLR)),
7. The navy dotted–dashed curve stands for the external inverse Compton from the dusty (EC (DT)),
8. The cyan curve stands for the combinations of upper spectra.

Table 7
The Modeling Parameters for 3C 454.3

State (1)	Value (2)	Unit (3)
The jet form description	...	...
Magnetic field strength: B	38	G
Bulk Lorentz Factor: Γ	22	⋯
Viewing angle: θ	0.1	⋯
Size of the emission region: R	6.0×10^{15}	cm
Redshift: z	0.859	⋯
The $n(\gamma)$ form description	...	...
The number density of electrons, N	800	cm^{-3}
Minimum Lorentz factor: $\gamma_{\min}$	1	⋯
Maximum Lorentz factor: $\gamma_{\max}$	1×10^7	⋯
Pivot energy of the electron spectrum: γ_0	180	⋯
Spectral curvature: r	1.8	⋯
Spectral index: s	4.8	⋯
The emission scenario form description	...	...
Luminosity of accretion disk: $L_{\rm disk}$	8.0×10^{46}	erg s^{-1}
Temperature of accretion disk: $T_{\rm disk}$	1.4×10^4	K
Accretion rate: a_e	0.1	⋯
Inner radius of BLR: $R_{\rm BLR}$	1×10^{17}	cm
Outer radius of BLR: $R_{\rm BLR}$	5.8×10^{17}	cm
Optical depth of BLR: $\tau_{\rm BLR}$	0.2	⋯
Position of the emission region: R_H	8.0×10^{16}	cm
Temperature of dust torus: $T_{\rm DT}$	100	K
Radius of dust torus: $R_{\rm DT}$	1×10^{18}	cm
Optical depth of dust torus: $\tau_{\rm DT}$	0.2	⋯

5. Discussions and Conclusions

5.1. Intraday Optical Variabilities

There are many theoretical models used to explain these variations, for example, the shocks propagating along the relativistic jets (Marscher & Gear 1985; Wagner & Witzel 1995) and hotspots or disturbances on or above accretion disks surrounding the black holes (Chakrabarti & Wiita 1993; Mangalam & Wiita 1993).

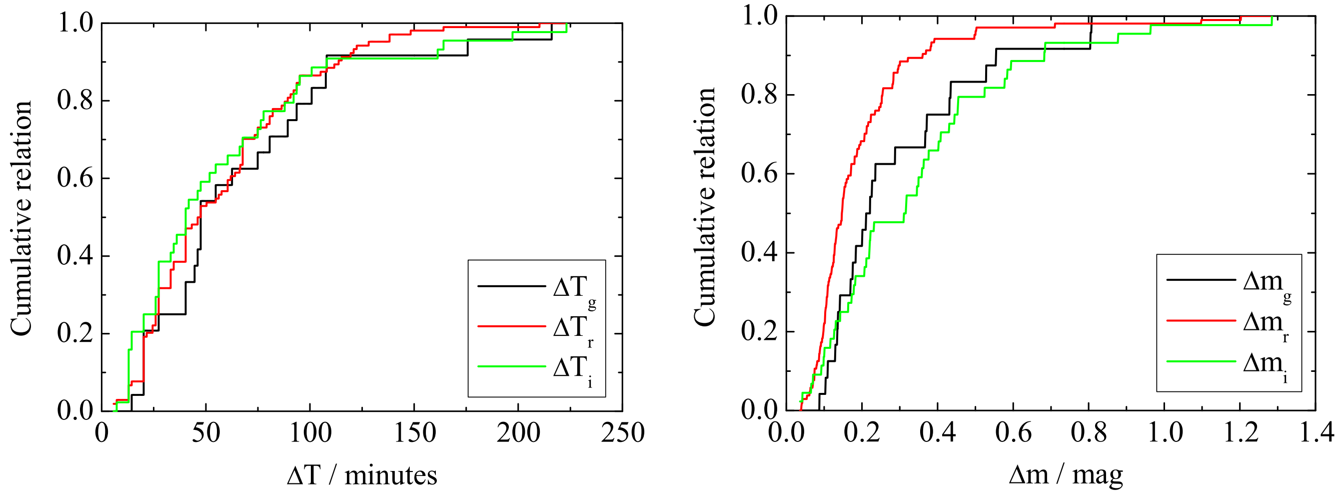

Figure 12. The comparisons between intraday variable timescales (ΔT) and variable values (Δm) at different bands. The black, red, and green lines stand for the results from the g band, r band, and i band respectively.

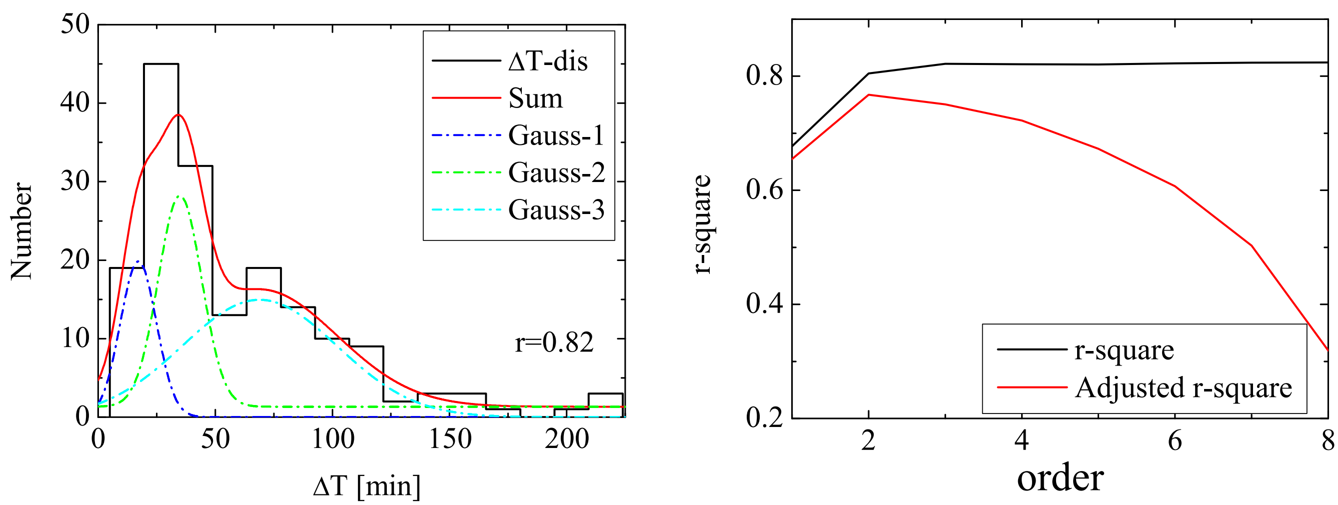

Figure 13. The distributions of ΔT. The left panel stands for the ΔT distributions and Gaussian fitting, and the right panel stands for the distributions of the correlation coefficient (r) from different order Gaussian functions.

In this work, we use the 1.26 m NGT to monitor the FSRQ 3C 454.3. During our monitoring, we find IDVs at three bands and calculate the variable timescales (ΔT) and variability amplitude (Δm). At the g band, ΔT ranges from 14.40 to 216 minutes; at the r band, ΔT ranges from 5.76 to 210.24 minutes; at the i band, ΔT ranges from 7.2 to 223.20 minutes.

We use a K-S test to compare the distributions of variable timescales (ΔT) and variability amplitude (Δm). For the variable timescales (ΔT), the analyzed results have been shown in Figure 12 (the left panel), and the chance probability for any two distributions to be from the same distributions are 75.6% between the g band and the r band, 43.9% between the g band and the i band, and 42.5% between the r band and the i band. From these results, we can find that the ΔT distributions from different bands are consistent with each other.

The analyzed results of Δm are shown in Figure 12 (the right panel), and the chance probability from the same distributions are 4.23% between the g band and the r band, 58.6% between the g band and the i band, and 0.004% between the r band and the i band. Based on these results, at the g and r band, Δm display the same distributions; but, the distributions from the r band are different from the other two bands. A possible reason for the r-band distribution of Δm being different from those of the i and g bands is that the sensitivity of CCD in the r band is higher than in the other two bands. The typical errors of our observations in the r band are about 0.02 mag, but the typical errors are about 0.05 mag in the g band and 0.09 mag in the i band.

We combine the variable timescales (ΔT) from the three bands into a sample, and analyze the distributions, seeing the left panel of Figure 13 (the black line). When we use the multiorder Gaussian function to fit the ΔT distributions, we adjust the order by comparing the correlative coefficient (r) and adjusted corrective coefficient (adjusted R). The variation trends of r (adjusted r) with the order are shown in Figure 13. The results show that when the order is 2 or 3, the fitting function is very suitable. So we choose the three-order Gaussian function to make the fitting, seeing the left panel of

Figure 13 (the green, green, and cyan lines), and the fitting function is

$$F(x) = 1.33 + 19.84 \times e^{-\left(\frac{x-17.18}{10.92}\right)^2} + 26.89 \times e^{-\left(\frac{x-34.91}{13.09}\right)^2} + 14.95 \times e^{-\left(\frac{x-68.92}{46.77}\right)^2},$$

with $r = 0.82$ and the adjusted $r = 0.75$.

The fitting results imply that the ΔT distribution has three components, and the center values are $\Delta T_1 = 17.18$ minutes, $\Delta T_2 = 34.91$ minutes, and $\Delta T_3 = 68.92$ minutes.

5.2. Quasiperiodicity Properties

Up to now, there were many works in the study of long-term period of 3C 454.3. For example, Webb et al. (1988) used the B lightcurve during the period from 1971 to 1985 to obtain three quasiperiodicities, 0.8, 3.0, and 6.4 yr. Based on the B lightcurve (1900–1996), Su (2001) found a period of ~12.39 yr. Qian et al. (2007) analyzed the radio lightcurve and found a period of 12.8 yr. Based on the Schuster method, Volvach et al. (2013) found some periods, $P = 1.1 \pm 0.1$, 2.3 ± 0.2, 7.3 ± 0.7, and 14.8 ± 1.4 yr. Fan et al. (2021) reported three possible QPO signals $P_1 = 3.04 \pm 0.02$ yr, $P_2 = 1.66 \pm 0.06$ yr, and $P_3 = 1.20 \pm 0.03$ yr.

In this work, we adopted the periodic analysis for the R lightcurve from 1900 to 2018 and obtained a possible period of $P = 2.92 \pm 0.85$ yr, which is consistent with the results of 3.0 yr from Webb et al. (1988), Volvach et al. (2013), and Fan et al. (2021). But we did not find the period of ~12.34 yr. So, we should make the further collection and accumulation of observations data in a future study.

Many models have been proposed to explain the long-term period, which can be classed into two types, dynamical models and geometrical models (Liu & Wu 2002; Kushwaha 2020). The dynamical models show that the period is caused by the accretion dynamics in the supermassive binary black holes (Sillanpää et al. 1988; Lehto & Valtonen 1996; Valtonen et al. 2008), while the geometrical models consider that the period is caused by the Doppler boosted jet emission from the jet procession (Katz 1997; Villata et al. 1998; Britzen et al. 2018).

Qian et al. (2021) discussed the suggestion of a binary black hole system of 3C454.3, which produced the two relativistic jets. For a binary black hole system, if the semimajor axes are b_1 and b_2, the period can be calculated by Kepler's law,

$$P^2 = \frac{4\pi^2(b_1 + b_2)^3}{G(M + m)}, \quad (3)$$

which can be transformed as

$$P \sim 1.72(1 + z)M^{-1/2}r_{16}^{3/2}\left(1 + \frac{m}{M}\right)^{-1/2} yr. \quad (4)$$

Here, M and m are masses of the primary and secondary black hole, in units of $10^8 M_\odot$, P is the period, and G is the gravitational constant, the sum of semiaxes $r_{16} = a_1 + a_2$, in units of 10^{16} cm.

In this work, we avail the period of $P = 2.92 \pm 0.85$ yr, $z = 0.859$. Woo & Urry (2002) reported the primary black hole mass $M \approx 1.5 \times 10^9 M_\odot$, and the secondary black hole mass $m = 1.86 \times 10^8 M_\odot$. So the sum of semiaxes can be written as

$$r_{16} = 2.32\left(1 + \frac{m}{M}\right)^{1/3} \approx 2.41.$$

Kraft et al. (1962) proposed that the orbit of a binary hole system should evolve through the gravitational radiation, and the lifetime should be

$$t_{\rm merge} = \frac{5}{256}\frac{c^5}{G^3}\frac{r^4}{(M + m)^2\mu}.$$

Here, $\mu = \frac{Mm}{M+m}$. Based on $r = 2.41 \times 10^{16}$ cm, we can obtain $t_{\rm merge} = 6.69 \times 10^3$ yr.

For a close binary black hole system, the luminosity of gravitational wave (L_G) can be calculated by Shapiro & Teukolsky (1983),

$$L_G = \frac{32}{5}\mu^2\frac{(M + m)^3}{r^5}\frac{G^4}{c^5}.$$

We can obtain $L_G = 1.56 \times 10^{48}$ erg s^{-1}.

5.3. Conclusion

In this work, we reported the observations of 3C454.3, which were monitored by the 1.26 m telescope in NGT. There are 6701 observations at the g, r and i bands. Our main conclusions are as follows.

1. Our monitoring period was from 2016 October 17 to 2018 December 14, and the largest variabilities are $\Delta m_g = 2.81 \pm 0.12$ mag at the g band, $\Delta m_r = 2.37 \pm 0.16$ mag at the r band, and $\Delta m_i = 3.13 \pm 0.07$ mag at the i band.
2. We analyze the distributions of variable timescales (ΔT) and find that there lie three denser regions. This result implies that the IDVs might have different origins.
3. Based on the long-term lightcurves, we used three methods (JV, REDFIT, and WWT) to obtain a weak period of $P = 2.92 \pm 0.85$ yr. We could not confirm suggestions made earlier of another possible period around 12.34 yr, which might be checked by extensive further observations of 3C 454.3. So, we should make further observations on this issue.

Thanks to the anonymous reviewer for the good suggestion. The work is partially supported by the National Natural Science Foundation of China (NSFC U1831119, NSFC U2031201, NSFC 11733001). The observations are monitored by the 1.26 m NGT telescope, which is located at the Xinglong Observatory of the National Astronomical Observatories. This paper has made use of up-to-date SMARTS optical/near-infrared lightcurves that are available at www.astro.yale.edu/smarts/glast/home.php. Data from the Steward Observatory spectropolarimetric monitoring project were used. This program is supported by Fermi Guest Investigator grants NNX08AW56G, NNX09AU10G, NNX12AO93G, and NNX15AU81G.

ORCID iDs

Y. H. Yuan https://orcid.org/0000-0001-8395-1706
G. G. Wang https://orcid.org/0000-0002-8032-4640
J. H. Fan https://orcid.org/0000-0002-5929-0968

References

Amaya-Almazán, R. A., Chavushyan, V., Patiño-Álvarez, V. M., et al. 2021, ApJ, 906, 5
Angel, J. R. P., & Stockman, H. S. 1980, ARA&A, 18, 321
Angione, R. J. 1968, PASP, 80, 339
Angione, R. J. 1971, AJ, 76, 412
Bachev, R., Semkov, E., Strigachev, A., et al. 2011, A&A, 528, 10
Bennett, A. S. 1962, MmRAS, 68, 163
Bennett, C. L., Hill, R. S., Hinshaw, G., et al. 2003, ApJS, 148, 97
Blom, J. J., Bloemen, H., Bennett, K., et al. 1995, A&A, 295, 330
Britzen, S., Fendt, C., Witzel, G., et al. 2018, MNRAS, 478, 3199
Chakrabarti, S. K., & Wiita Paul, P. J. 1993, ApJ, 411, 602
Costamante, L, Cutini, S, Tosti, G, Antolini, E, & Tramacere, A 2018, MNRAS, 477, 4749
de Diego, J. A. 2010, AJ, 139, 1269
de Diego, J. A., Polednikova, J., Bongiovanni, A., et al. 2015, AJ, 150, 44
Fan, J. H. 2005, ChJAS, 5, 213
Fan, J. H., Kurtanidze, O., Liu, Y., et al. 2014a, ApJS, 213, 26
Fan, J. H., Kurtanidze, O., Liu, Y., et al. 2017, ApJ, 837, 45
Fan, J. H., Kurtanidze, O., Nikolashvili, N. G., et al. 2004, ChJA&A, 4, 133
Fan, J. H., Kurtanidze, S. O., Liu, Y., et al. 2021, ApJS, 253, 10
Fan, J. H., Yuan, Y. H., Wu, H., et al. 2019, RAA, 19, 142
Fan, X.-L., Li, S.-K., Liao, N.-H., et al. 2018, ApJ, 856, 80
Fiorucci, M., Tosti, G., & Rizzi, N. 1998, PASP, 110, 105
Foster, G. 1996a, AJ, 112, 1709
Foster, G. 1996b, AJ, 111, 541
Fuhrmann, L., Cucchiara, A., Marchili, N., Tosti, G., et al. 2006, A&A, 445, 1
Gaur, H., Gupta, A., & Wiita, P. J. 2012, AJ, 143, 23
Giommi, P., Blustin, A. J., Capalbi, M., et al. 2006, A&A, 456, 911
Gu, M. F., Lee, C. U., Pak, S., et al. 2006, A&A, 450, 39
Hartman, R. C., Bertsch, D. L., Bloom, S. D., et al. 1999, ApJS, 123, 79
Heidt, J., & Wagner, S. J. 1996, A&A, 305, 42
Hovatta, T., Valtaoja, E., Tornikoski, M., & Lähteenmäki, A. 2009, A&A, 494, 527
Jackson, N., & Browne, W. A. 1991, MNRAS, 250, 414
Jurkevich, I., Usher, P. D., & Shen, B. S. P. 1971, Ap&SS, 10, 402
Katz, J. I. 1997, ApJ, 478, 527
Kidger, M., Takalo, L., & Sillanpaa, A. 1992, A&A, 264, 32
Kinzel, W. M., Dickman, R. L., & Predmore, C. R. 1988, Natur, 331, 48
Kraft, R. P., Mathews, J., & Greenstein, J. L. 1962, ApJ, 136, 312
Kurtanidze, O. M., Tetradze, S. D., Richter, G. M., et al. 2009, in ASP Conf. Ser. 408, The Starburst-AGN Connection, ed. W. Wang et al. (San Francisco, CA: ASP), 266
Kushwaha, P. 2020, Galax, 8, 15K
Lehto, H. J., & Valtonen, M. J. 1996, ApJ, 460, 207
Liu, F. K., & Wu, X. B. 2002, A&A, 388, 48
Liu, X. L., Yuan, Y. H., & Huang, H. R. 2021, RAA, 21, 102
Lloyd, C. 1984, MNRAS, 209, 69
Lomb, N. R. 1976, Ap&SS, 39, 447
Mangalam, A. V., & Wiita, P. J. 1993, ApJ, 406, 420
Marscher, A. P., & Gear, W. K. 1985, ApJ, 298, 114
Massaro, E., Tramacere, A., & Perri, M. 2006, A&A, 448, 861
Ogle, P. M., Wehrle, A. E., Balonek, T., et al. 2011, ApJS, 195, 19
Pian, E., Foschini, L., Beckmann, V., Soldi, S., et al. 2006, A&A, 449, 21
Qian, S. J., Britzen, S., Krichbaum, T. P., et al. 2021, A&A, 653, A7
Qian, S. J., Kudryavtseva, N. A., Britzen, S., et al. 2007, ChJAA, 3, 364
Raiteri, C. M., Ghisellini, G., Villata, M., et al. 1998b, A&AS, 127, 445
Raiteri, C. M., Villata, M., Larionov, V. M., et al. 2007, A&A, 473, 819
Raiteri, C. M., Villata, M., Larionov, V. M., et al. 2008, A&A, 491, 755
Raiteri, C. M., et al. 1998a, A&AS, 130, 495
Romero, G. E., Cellone, S. A., & Combi, J. A. 1999, A&AS, 135, 477
Sahakyan, N. 2021, MNRAS, 504, 5074
Sandage, A. 1966, ApJ, 144, 1234
Sarkar, A., Gupta, A. C., Chitnis, V. R., et al. 2021, MNRAS, 501, 50
Scargle, J. D. 1982, ApJ, 263, 835
Schulz, M., & Mudelsee, M. 2002, CG, 28, 421
Shapiro, S. L., & Teukolsky, S. A. 1983, Black Holes, White Dwarfs, and Neutron Stars (Wiley-Interscience: New York), 476
Sillanpää, A., Haarala, S., & Korhonen, T. 1988, A&AS, 72, 347
Smith, P. S., & Balonek, T. J. 1998, PASP, 110, 1164
Stickel, M., Fried, J. W., Kuehr, H., Padovani, P., & Urry, C. M. 1991, ApJ, 374, 431
Su, C. Y. 2001, ChA&A, 25, 153
Tao, J., Fan, J., Qian, B., & Liu, Y. 2008, AJ, 135, 737
Tavecchio, F., Maraschi, L., Ghisellini, G., et al. 2002, ApJ, 575, 137
Tramacere, A., Giommi, P., Perri, M., et al. 2009, A&A, 501, 879
Tramacere, A., Massaro, E., & Taylor, A. M. 2011, ApJ, 739, 66
Tritton, K. P., & Selmes, R. A. 1971, MNRAS, 153, 453
Ulrich, M. H., Maraschi, L., & Urry, C. M. 1997, ARA&A, 35, 445
Urry, C. M., & Padovani, P. 1995, PASP, 107, 803
Valtaoja, E., Lehto, H., Teerikorpi, P., et al. 1985, Natur, 314, 148
Valtonen, M., Kidger, M., Lehto, H., & Poyner, G. 2008, A&A, 477, 407
Vaughan, S., Uttley, P., Markowitz, A. G., et al. 2016, MNRAS, 461, 3145
Vercellone, S., D'Ammando, F., Vittorini, V., et al. 2010, ApJ, 712, 405
Villata, M., Raiteri, C. M., & Balonek, T. J. 2006, A&A, 453, 817
Villata, M., Raiteri, C. M., Sillanpää, A., et al. 1998, MNRAS, 293, 13
Villata, M., Raiteri, C. M., Sobrito, G., et al. 2001, ApL&C, 40, 123
Visvanathan, N., & Elliot, J. L. 1973, ApJ, 179, 721
Vittorini, V., Tavani, M., Cavaliere, A., et al. 2014, ApJ, 793, 98
Volvach, A. E., Volvach, L. N., Larionov, M. G., et al. 2013, ARep, 57, 34
Wagner, S. J., & Witzel, A. 1995, ARA&A, 33, 163
Weaver, Z. R., Balonek, T. J., Jorstad, S. G., et al. 2019, ApJ, 875, 15
Webb, J. R., Smith, A. G., Leacock, R. J., et al. 1988, AJ, 95, 374
Woo, J. H., & Urry, C. M. 2002, ApJ, 579, 530
Xie, G. Z., Li, K. H., Bai, J. M., et al. 2001, ApJ, 548, 200
Xiong, D., Bai, J., Zhang, H., et al. 2017, ApJS, 229, 21
Yuan, Y. H., & Fan, J. H. 2021, PASP, 133, 074101
Zhang, S., Collmar, W., & Schönfelder, V. 2005, A&A, 444, 767